Adaptive framework for robust high-resolution image reconstruction in multiplexed computational imaging architectures

Noha A. El-Yamany,* Panos E. Papamichalis, and Marc P. Christensen

Department of Electrical Engineering, Southern Methodist University, P.O. Box 750338, Dallas, Texas 75275, USA

*Corresponding author: nelyaman@smu.edu

Received 11 September 2007; revised 23 January 2008; accepted 25 February 2008; posted 25 February 2008 (Doc. ID 87399); published 1 April 2008

In multiplexed computational imaging schemes, high-resolution images are reconstructed by fusing the information in multiple low-resolution images detected by a two-dimensional array of low-resolution image sensors. The reconstruction procedure assumes a mathematical model for the imaging process that could have generated the low-resolution observations from an unknown high-resolution image. In practical settings, the parameters of the mathematical imaging model are known only approximately and are typically estimated before the reconstruction procedure takes place. Violations to the assumed model, such as inaccurate knowledge of the field of view of the imagers, erroneous estimation of the model parameters, and/or accidental scene or environmental changes can be detrimental to the reconstruction quality, even if they are small in number. We present an adaptive algorithm for robust reconstruction of high-resolution images in multiplexed computational imaging architectures. Using robust M-estimators and incorporating a similarity measure, the proposed scheme adopts an adaptive estimation strategy that effectively deals with violations to the assumed imaging model. Comparisons with nonadaptive reconstruction techniques demonstrate the superior performance of the proposed algorithm in terms of reconstruction quality and robustness.

OCIS codes: 110.1758, 100.2980.

1. Introduction

The production of high-resolution (HR) images has attracted much attention recently in diverse fields ranging from consumer electronics and medical imaging to surveillance and military applications. HR images can be produced with high-precision optical sensors that are, however, limited by their high cost, bulky form factor, and noise level. Signal processing offers inexpensive alternative solutions for the reconstruction of such HR images from multiple low-resolution (LR) images. These solutions have resulted in two fields that have attracted much research activity in the past few decades, that is, multiplexed computational imaging (MCI) [1–9] and multiframe superresolution (SR) [10–34]. In multiframe SR, spatial resolution enhancement is achieved by combining the information in a sequence of subpixel-shifted LR frames. The relative motion between the LR frames is a result of the camera movement, object(s) motion in the scene and/or both. On the other hand, in MCI, HR images are produced by fusing the information in multiple LR images captured by a two-dimensional array of LR image sensors with their fields of view (FOVs) overlapping and having appropriately selected relative positions from each other. MCI has benefited from the algorithms developed in the literature for multiframe SR reconstruction due to the similarities between the two problems [3].

MCI schemes with either fixed or flexible architectures enable the design of cameras of a flat form factor [3–8]. TOMBO [4] (thin observation module by bound optics) is an example of a MCI scheme with fixed geometry in which a conventional sensor array is divided into pixel subarrays. With the object distance fixed, a

0003-6935/08/10B117-11$15.00/0

specific resolution enhancement can be achieved. This fixed geometry, however, dictates the optimization of the design for a specific resolution and FOV, which limits the design utility. Flexible and steerable architectures, such as PANOPTES [5–7] (processing arrays of Nyquist limited observations to produce a thin electro-optic sensor), are highly desired to overcome this fundamental limitation and to increase the utility of the designed flat imaging sensor. PANOPTES is an adaptive, multiresolution, and attentive flat computational imaging sensor that interrogates all the regions of interest in the scene and adaptively directs its resources (subimagers) to these regions of interest based on the information content distribution of the scene [5–7]. In this architecture, subimagers (SIs) are adaptively allocated to the scene such that more SIs are steered to regions of interest with high information content and fewer SIs are steered to regions of less importance or lower information content. This is achieved by an information-theory driven feedback mechanism that controls microelectromechanical mirror arrays in the sensor pupil plane to vary the FOVs of the SIs [5–7]. We are particularly interested in HR image reconstruction in steerable MCI architectures such as PANOPTES, as the inherent steering capability of the architecture will likely induce errors in the anticipated look direction, and hence a robust algorithm that is tolerant to such errors is a necessity. It is worth mentioning, however, that the proposed algorithm can also be applied to fixed MCI architectures.

Algorithms devoted to HR image reconstruction in MCI generally assume a mathematical model for the imaging process that could have generated the LR images detected by the array of image sensors from an unknown HR image. The model parameters represent the image acquisition geometry, the behavior of the optical elements, the integration and sampling effects of the detector, and the relative physical positions and sizes of the detector pixels [8]. In practical settings, these parameters are known only approximately and are typically estimated prior to the reconstruction process. Inaccurate calibration or steering of the imagers, erroneous estimation of the model parameters, and/or accidental scene or environmental changes could be detrimental to the reconstruction process and could result in poor HR estimates. In addition, in MCI schemes that employ high degrees of optical diversity [3,8], the number of the model parameters increases and hence the associated uncertainty in their estimates increases as well. Therefore, reconstruction algorithms that are robust to deviations in the parameters of the assumed mathematical model are necessary.

Robust statistics [35–39] has emerged as a family of theories and techniques for estimation while dealing with deviations from idealized model assumptions. In particular, robust M-estimation has been found to be effective in many computer vision applications such as optical flow estimation [40], robust denoising [41], and robust anisotropic diffusion [42]. Robust M-estimation has been explored recently in multiframe SR. Capel [26] used Huber functions in the prior term within the context of maximum *a posteriori* (MAP) estimation. El-Yamany and Papamichalis [28–31] developed an adaptive M-estimation scheme without regularization using the Lorentzian error norm in the data fidelity term. Patanavijit and Jitapunkul [27] also demonstrated the use of the Lorentzian error norm in both the data fidelity and the regularization terms of the objective function. Pham *et al.* [32] introduced a robust M-estimation scheme for multiframe SR without regularization, where the Gaussian error norm is used. Here we describe an adaptive algorithm for reconstruction of HR images in steerable MCI architectures in a robust M-estimation framework. Using robust M-estimators and incorporating a similarity measure, the proposed algorithm adopts an adaptive estimation strategy that effectively deals with violations to the assumed imaging model.

In Section 2 we introduce the mathematical imaging model. In Section 3 we develop the proposed adaptive reconstruction algorithm, and its performance is then evaluated through experimental results in Section 4. In Section 5 we conclude the paper and discuss ongoing related work.

2. Observation Model

In a MCI scheme consisting of an array of SIs, we assume the following linear observation model in which the LR images detected by the SIs are assumed to have been obtained from the unknown HR scenery by geometric warping, blurring, and sampling processes:

$$\mathbf{Y}_k = D_k H_k F_k \mathbf{X} + \mathbf{N}_k, \qquad k = 1, 2, \ldots, L, \tag{1}$$

where L is the total number of SIs in the sensor array; $\mathbf{Y}_k$ and $\mathbf{X}$ are the LR images detected by the kth SI, SI_k, and the unknown HR image, respectively. It is worth noting that in Eq. (1), images are represented by vectors that are obtained by lexicographic ordering of two-dimensional images. The matrices D_k and H_k represent the spatial subsampling at the detector and the point-spread function (PSF), respectively. F_k is the warping matrix that represents the relative position between SI_k and the unknown HR image ($\mathbf{X}$). The sampling factor represented by D_k is assumed to be the same in both the x and the y directions. $\mathbf{N}_k$ is the additive noise term associated with SI_k. Figure 1 illustrates the sequence of operations of the assumed imaging model in Eq. (1). Here we only consider dealing with an identical optical system, i.e., $D_k = D$, $H_k = H \,\forall\, k$. In this case, the model in Eq. (1) can be simplified to

$$\mathbf{Y}_k = DHF_k \mathbf{X} + \mathbf{N}_k, \qquad k = 1, 2, \ldots, L. \tag{2}$$

In addition, the PSF is assumed to be space invariant. It is worth mentioning that, in the proposed reconstruction algorithm, matrices D, H, and F_k are not physically constructed. Instead, their functions

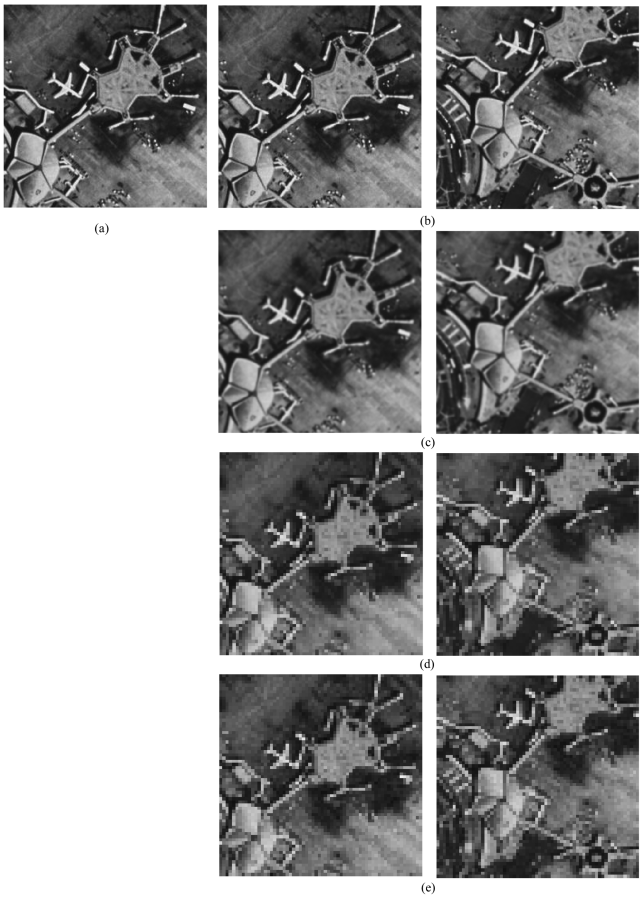

Fig. 1. Sequence of operations of the imaging model in Eq. (1): (a) original HR image, (b) geometric warping, (c) blurring, (d) sampling, (e) noise addition. Middle column, reference SI; right column, SI with a relative rotation and offset with respect to the reference SI.

are performed as simple image processing operations such as downsampling, convolving with a blurring kernel, and geometric warping, respectively [16–18,21,22,27–32]. This approach significantly reduces the computational load associated with the construction of these matrices, which are typically sparse and of very high dimensionality. The relative position of SI_k is defined with respect to a reference subimager SI_1 and is represented by an affine transformation in the following form [3]:

$$\begin{bmatrix} x' \\ y' \end{bmatrix} = s_k \begin{bmatrix} \cos\theta_k & -\sin\theta_k \\ \sin\theta_k & \cos\theta_k \end{bmatrix} \begin{bmatrix} x \\ y \end{bmatrix} + \begin{bmatrix} u_k \\ v_k \end{bmatrix}. \quad (3)$$

The parameters s_k, θ_k, u_k, and v_k represent the magnification (zooming) factor, the rotation angle, the shift in the x direction, and the shift in the y direction, respectively, of SI_k with respect to the reference SI; u_k and v_k are measured in fractional pixel shifts in the LR image grid. The set of affine transformation parameters collectively define the degrees of optical diversity in a MCI architecture [3,8].

3. Adaptive Reconstruction Algorithm

A. Problem Formulation

Following the observation model in Eq. (2) and recasting the reconstruction problem within the generalized M-estimation framework, the HR image estimate is the solution of the following minimization problem:

$$\mathbf{X}^* = \arg\min_{\mathbf{X}} \sum_{k=1}^{L} \rho(DHF_k\mathbf{X} - \mathbf{Y}_k) = \arg\min_{\mathbf{X}} \sum_{k=1}^{L} \rho(\mathbf{E}_k), \quad (4)$$

where $\mathbf{E}_k$ is the vector of the projection errors corresponding to the kth LR image, and ρ is an even-symmetric function that has a unique minimum at zero and satisfies the following condition:

$$\frac{\partial}{\partial \mathbf{X}} \sum_{k=1}^{L} \rho(\mathbf{E}_k) = \mathbf{0} \Rightarrow \sum_{k=1}^{L} (DHF_k)^T \psi(\mathbf{E}_k) = \mathbf{0}, \quad (5)$$

where $\rho(\mathbf{E}) = \sum_j \rho(e_j)$ and $\psi(\mathbf{E}) = [\psi(e_1) \ . \ . \ \psi(e_j)..]^{\mathbf{T}}$. $\rho(e_j)$ is a function applied to the element e_j of $\mathbf{E}$, and $\psi(e)$ is the first derivative of ρ with respect to e and is referred to as the influence function [35–37].

The mathematical model in Eq. (2) is only an approximation to the real imaging process. Deviations from the idealized model assumptions and inaccurate estimates of its parameters could be detrimental to the reconstruction process and could result in poor HR estimates. We leverage tools from robust M-estimation [35–37] in an attempt to address the robustness of HR image reconstruction in MCI schemes. The proposed approach was first introduced within the context of multiframe SR in Refs. [28–31]. Because of the strong similarity between MCI and multiframe SR, the proposed algorithm can be applied in a straightforward manner to multiplexed computational imaging schemes.

B. Objective Function

The robustness of HR image reconstruction has been addressed recently in the literature within the context of multiframe SR [19,21–34]. In the M-estimation framework, the solution of Eq. (4) has been formulated as a least-squares (LS) estimation problem using the L_2 error norm [18]. However, LS estimation exhibits poor performance in the presence of deviations from the model assumptions (outliers) [21,22,26–33]. The nonrobustness of the L_2 error norm lies in its influence function (i.e., its first derivative), which is linear and increases without bound assigning large weights to large errors that typically occur as a result of violations to the assumed imaging model. To achieve a robust SR reconstruction, Farsiu *et al.* [21,22] proposed the use of the L_1 error norm as a robust alternative to the L_2 error norm. However, the L_1 influence function is the signum function. Therefore, all errors (small or large) are assigned the same weights +1 or −1, depending only

on their sign. The L_1 error norm is more robust than the L_2 in the presence of outliers because of its bounded influence. However, because of its constant-valued influence function that does not differentiate between small and large errors, the resulting SR estimates suffer from various reconstruction artifacts, especially in the absence of a regularization term in the objective function [28–31]. Figure 2. depicts plots of the L_2 and L_1 error norms and their corresponding influence functions in the one-dimensional case.

In the proposed approach we introduce the use of robust error norms in the objective function, in particular, the robust error norms that correspond to a specific class of M-estimators known as redescending M-estimators [35–37]. For these estimators, the influence function ψ increases up to a point, which is referred to as the outlier threshold, after which it decreases (redescends) as the error grows. Because of this behavior, large errors that fall beyond the outlier threshold are assigned weights that decrease as the error increases, thus providing a soft outlier rejection rule. Of all the redescending M-estimators we are particularly interested in estimators whose influence functions are differentiable and have only one parameter, which will be determined from observations shown later. Examples of these estimators are the Lorentzian (Cauchy), Geman and McClure, Gaussian (Welsch), and Tukey's biweight [35–42]. Here we only demonstrate the Lorentzian estimator whose error norm is defined as

$$\rho(e;\tau) = \log[(e^2 + \tau^2)/\tau^2], \tag{6}$$

where e and τ are the error and the outlier threshold,

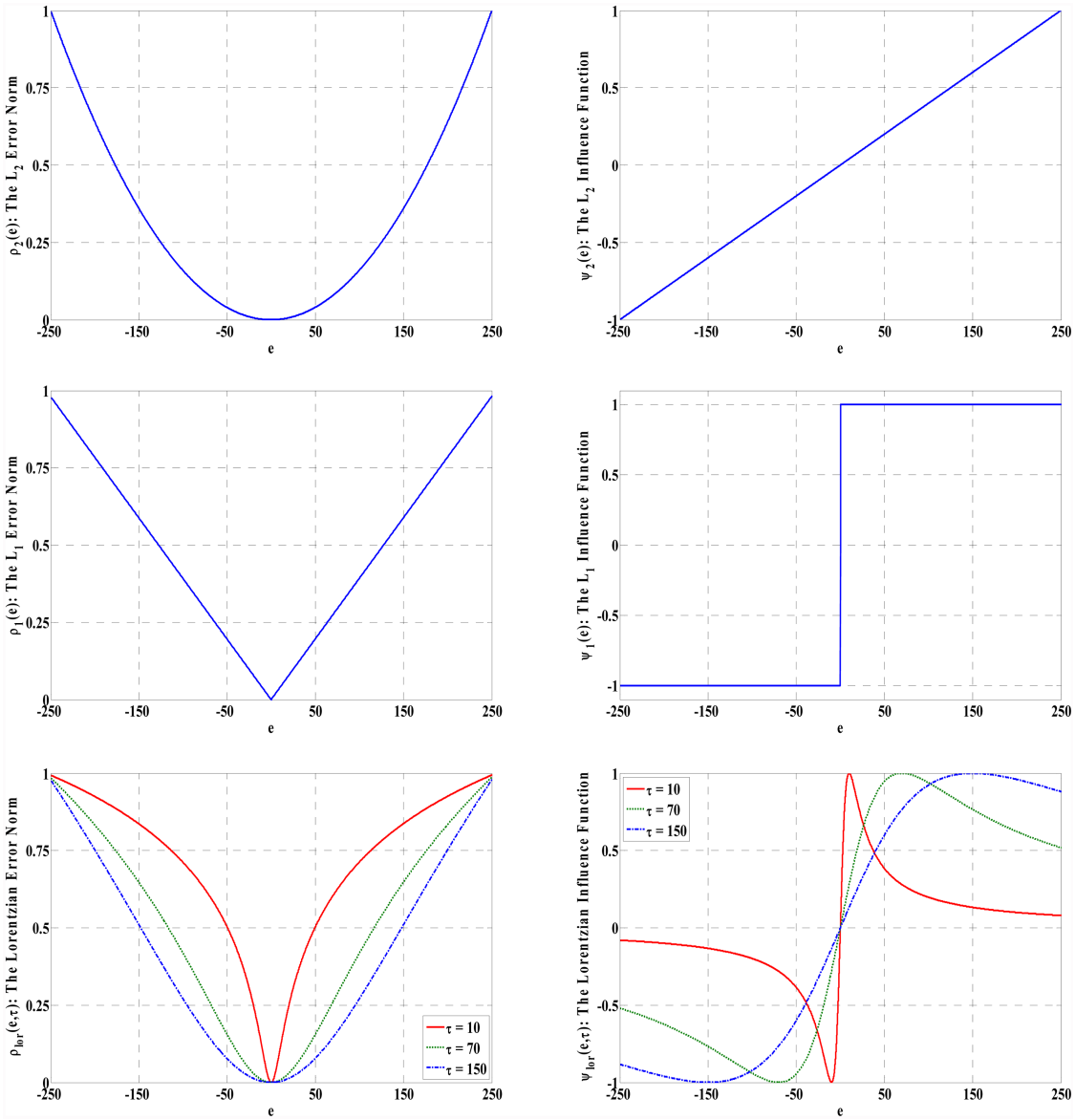

Fig. 2. (Color online) Plot of the error norms (left) and influence functions (right) for the L_2, L_1, and Lorentzian error norms. All the plots are normalized to illustrate the relative weight assigned to the errors.

respectively. The Lorentzian influence function [which is proportional to the first derivative in Eq. (6)] is given by

$$\psi(e;\tau) = 2\tau e/(e^2+\tau^2). \tag{7}$$

The influence function in Eq. (7) is scaled to have a maximum influence of unity independent of the outlier threshold value. This normalization is particularly important in the proposed adaptive formulation to ensure that all influence functions have the same weight at their respective outlier thresholds, as will be shown later. Figure 2 depicts plots of the Lorentzian error norm and its influence function for different values of τ in the one-dimensional case. From these plots it is shown how the influence function decreases faster for smaller τ, assigning lower weights to the errors that fall beyond the outlier threshold.

Recasting the HR reconstruction problem in an adaptive M-estimation framework by use of redescending M-estimators, the HR estimate is given by

$$\begin{aligned}\mathbf{X}^* &= \arg\min_{\mathbf{X}} \sum_{k=1}^{L} \rho(DHF_k\mathbf{X} - \mathbf{Y}_k;\tau_k) \\ &= \arg\min_{\mathbf{X}} \sum_{k=1}^{L} \rho(\mathbf{E}_k;\tau_k),\end{aligned} \tag{8}$$

where $\rho(\mathbf{E}_k;\tau_k)$ is the robust error norm associated with the kth SI, and τ_k is the corresponding outlier threshold. As shown in Eq. (8), instead of the typical M-estimation approach to the problem of HR image reconstruction in which the same error norm would be used for all the SIs, we propose the use of a different error norm (with a different outlier threshold) for each LR image (SIs). This formulation effectively deals with deviations from the assumed imaging model that might occur in individual SIs, especially in steerable MCI architectures, as a result of inaccurate calibration or steering of the SIs, incorrect estimation of their relative positions, and/or accidental changes in the setup. The robustness of the proposed scheme will be demonstrated in the set of experiments presented later.

C. Update Equation

To determine the solution for Eq. (8), one might use Newton's algorithm. However, the influence function of redescending M-estimators is bounded (as shown in Fig. 2), and its derivative is not always positive and goes to zero at infinity, which makes using Newton's algorithm unreliable and convergence is not guaranteed [37]. We chose to use the gradient descent method, and the update equation that minimizes Eq. (8) can be written as

$$\mathbf{X}^{n+1} = \mathbf{X}^n - \eta \sum_{k=1}^{L} \nabla\rho(\mathbf{E}_k^n;\tau_k), \qquad n = 0,1,2,..., \tag{9}$$

where η is the step size. It can be shown that Eq. (9) can be simplified to

$$\mathbf{X}^{n+1} = \mathbf{X}^n - \eta \sum_{k=1}^{L} (DHF_k)^T \psi_k^n, \qquad n = 0,1,2,..., \tag{10}$$

where ψ_k^n is a vector whose jth element is $\psi(e_{j,k}^n;\tau_k)$, the Lorentzian influence function evaluated at $e_{j,k}^n$ (the jth element in $\mathbf{E}_k^n$). The choice of the step size parameter (η) plays an important role in the convergence behavior of the gradient descent method. If the step size is too large, divergence will occur; if the step size is too small, the rate of convergence could be very slow [43]. Choosing a constant step size is the simplest approach. However, constant step size selection is useful only in cases in which an appropriate step size value is known or can be determined fairly easily [43]. For twice differentiable robust error norms, such as the Lorentzian, a proper constant step size selection can be obtained by use of the method of simultaneous overrelaxation (SOR) [40,41,44]. The SOR step size is defined as $\eta = \omega/T$, where ω is a constant such that $0 < \omega < 2$ and T is an upper bound on the second partial derivative of the $\rho(e;\tau)$ with respect to e. The exact choice of ω affects only the rate of convergence. In the proposed approach, ω is set to 1 and the step size is approximated by $\eta = 1/T \approx \tau/2$ for the Lorentzian error norm. To achieve fast convergence motivated by the SOR algorithm [40,41,44], we used a different step size for each L term in Eq. (10), i.e.,

$$\mathbf{X}^{n+1} = \mathbf{X}^n - \sum_{k=1}^{L} \eta_k (DHF_k)^T \psi_k^n, \qquad n = 0,1,2,..., \tag{11}$$

where the step size parameter η_k is calculated for the Lorentzian error norm as follows:

$$\eta_k = \tau_k/2 \tag{12}$$

Having set the adaptive step size as in Eq. (12), the convergence is also checked after each iteration. If the cost function does not improve, η_k can be reduced by a small amount (e.g., 5%); otherwise it is kept at its current value. In all the experiments we conducted, however, setting the step size as in Eq. (12) has shown fast convergence (typically from 7 to 12 iterations), and there was no need to reduce the step size calculated in Eq. (12). In all the experiments presented in this paper, the initial HR estimate was found through bilinear interpolation of the LR image detected by the reference subimager. We are currently investigating computationally efficient optimization techniques for minimization of the nonlinear objective function in Eq. (8).

D. Calculation of the Outlier Thresholds

The outlier threshold plays a vital role in dealing with the outliers in the estimation process. Its calculation can be done by use of statistical methods [35–37] or based on problem-dependent choices [37–42]. Within the proposed framework, we developed an adaptive strategy to estimate τ_k from the LR observations, which is described in what follows.

1. *Calculation of* τ_1

Since we are interested in increasing the resolution of a LR reference image ($\mathbf{Y}_1$) using the information in that image and the available LR images ($\mathbf{Y}_k$), the projection errors that correspond to the reference image should all be considered in the estimation process, i.e., they are all inliers. For 8 bit data, the maximum absolute value for the projection errors is 255; hence a reasonable choice for the outlier threshold for the reference SI, τ_1, is 255.

2. *Calculation of* τ_k

To compute the outlier thresholds for the rest of the SIs, a metric that measures the similarity between the reference image and the kth motion-compensated LR image ($\tilde{\mathbf{Y}}_k$) is first computed. This metric is denoted by $d_k = d(\mathbf{Y}_1, \tilde{\mathbf{Y}}_k)$, where $k = 2, 3, \ldots, L$. The outlier threshold for a given SI is then calculated as a function of this metric such that, if $d_k \to 0$, $\tau_k \to \tau_1$, and if $d_k \to d_{\max}$ (upper bound on d), $\tau_k \to \tau_{\min}$ (lower bound on τ). Under these constraints, we consider the following exponential function as a reasonable choice to calculate τ_k from d_k :

$$\tau_k = \tau_1 e^{-\alpha d_k} = 255 e^{-\alpha d_k}. \tag{13}$$

Parameter α in Eq. (13) controls the decay of the exponential function and, given the two constraints above, is calculated as

$$\alpha = \frac{1}{d_{\max}} \log\left(\frac{255}{\tau_{\min}}\right). \tag{14}$$

The lower bound on the outlier threshold ($\tau_{\min}$) is chosen to be an arbitrarily small number. In our experiments presented in this paper, $\tau_{\min}$ was set to 10^{-8}. For the similarity metric, we used the normalized average sum of absolute differences (SADs) between $\mathbf{Y}_1$ and $\tilde{\mathbf{Y}}_k$, which is defined by

$$d_k = \frac{1}{255 \times MN} \sum_{x=1}^{M} \sum_{y=1}^{N} |y_1(x,y) - \tilde{y}_k(x,y)|. \tag{15}$$

The normalized average SAD has an upper bound of unity. Therefore, α is computed as $\alpha = \log(255 \times 10^8) \approx 24$. The outlier threshold for the kth SIs is then computed as

$$\tau_k = 255 e^{-24 d_k}, \qquad k = 2, 3, \ldots, L, \tag{16}$$

where d_k is the normalized average SAD between the reference LR image ($\mathbf{Y}_1$) and the kth motion-compensated LR image ($\mathbf{Y}_k$). It is worth mentioning that the average SAD is one possible measure to assess the similarity between the reference LR image and each motion-compensated LR image. We chose this measure because of its low computational complexity, and it captures the mismatch between the two LR images well.

4. Experimental Results

We now evaluate the performance of the proposed algorithm through experimental simulations. The notation 4× HR image reconstruction will be used to denote an increase of the spatial resolution by a factor of 4 in both the x and the y directions. The performance of the proposed algorithm will be compared only with the methods in Refs. [18,22,27]. In all the experiments, the method of iterative gradient descent [43] is used, and the stopping criterion for all the algorithms was set to $\|\mathbf{X}^{n+1} - \mathbf{X}^n\|_2 / \|\mathbf{X}^n\|_2 \le 10^{-4}$.

A. Synthetic Experiment: 4× HR Reconstruction

In this experiment we assume that a region of interest (ROI) has been identified by the MCI system and that SIs will be steered toward that ROI to increase their spatial resolution. Furthermore, we assume that the steerable MCI system offers diversity only in the translational offsets between the SIs, i.e., SIs have translational offsets only with respect to a specified reference SI. Figures 3(a) and 3(b) depict the original 600 × 800 HR scene and a 256 × 256 ROI, respectively. Following the observation model in Eq. (2), a sequence of 16 LR images is generated from the HR ROI (this sequence will be referred to as test sequence #1) as follows. A set of 16 integer offsets (measured on the HR grid) to increase the resolution by a factor of 4 (assuming uniform sampling) is generated and the HR ROI is shifted by these offset values. The shift pairs are $\{(0,0), (0,1), (0,2), (0,3), (1,0), (1,1), (1,2), (1,3), (2,0), (2,1), (2,2), (2,3), (3,0), (3,1), (3,2), (3,3)\}$. Image #4 [offset of (0,3)] and image #10 [offset of (2,1)] are then rotated 10^0 clockwise and zoomed in by a factor of 1.2, respectively, to create a general affine position for SIs #4 and #10. The resulting 16 warped images are then convolved with a normalized 5 × 5 Gaussian kernel of zero mean and variance of 0.5, and downsampled by a factor of 4 in both the x and the y directions. A zero-mean Gaussian noise is then added to the resulting LR images such that each has a signal-to-noise ratio (SNR) of 30 dB. The SNR of each LR image in a synthetic experiment is defined as $\mathbf{SNR}(\mathbf{Y}_k) = 10\mathbf{log}_{10}[\mathbf{var}(\mathrm{DHF}_k\mathbf{X}^{\mathrm{original}})/\mathbf{var}(\mathbf{N}_k)]\,\mathbf{dB}$. Figures 3(c)–3(e), depict the LR images detected by SI #1 (the reference SI), SI #4, and SI #10, respectively. Although the relative offsets are known in this experiment, we used a spatial-domain motion estimation algorithm [45] to estimate the offsets between each SI and the reference SI (a global translational model is assumed). In this sense we have simulated modeling and motion estimation errors, since rota-

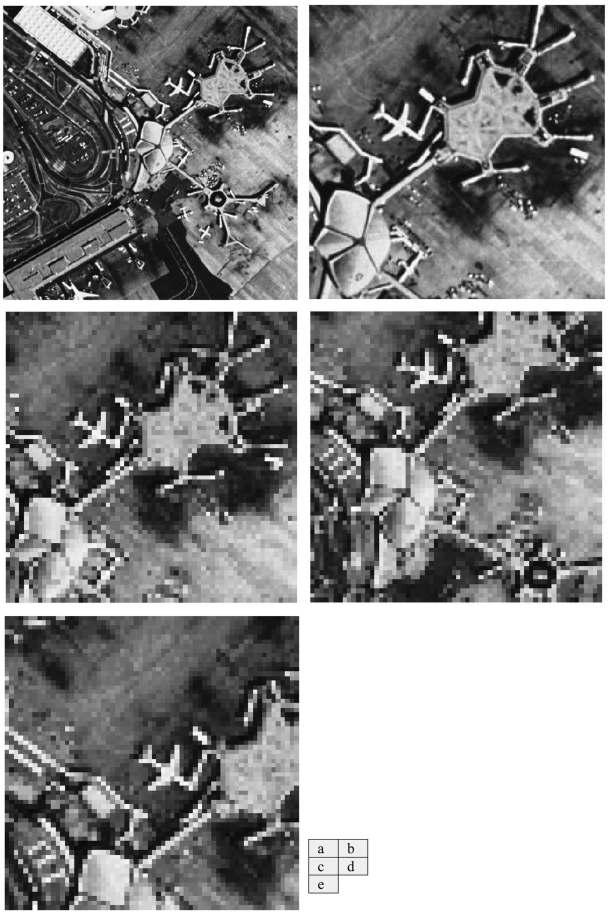

Fig. 3. Test sequence #1: a, original HR scene (600 × 800); b, HR region of interest (256 × 256); c, LR image detected by the reference subimager, SI #1; d, LR image detected by SI #4, which has a relative offset and rotation with respect to SI #1; e, LR image detected by SI #10, which has a relative offset and magnification with respect to SI #1.

tion and zooming components for SI #4 and SI #10 will be discarded by the motion estimation algorithm, and the offsets estimated for SI #4 and SI #10 will be incorrect because the corresponding images do not obey the global translational model. The motion estimation algorithm [45] produced shift values that are close to the true values for all SIs except SI #4 and SI #10 whose estimated shifts were $(28, -65)$ and $(67, 35)$, respectively. In addition to the above, a bias of 4 pixels (on the HR grid) is added to the relative offset estimated by the motion estimation algorithm [45] for SI #7 to simulate additional motion estimation errors. To simulate blur estimation errors, the PSF is assumed to be a normalized 5×5 Gaussian kernel of zero mean and unity variance. Figure 4 depicts plots of the average SAD (d_k), the outlier thresholds (τ_k), and the Lorentzian influence functions (ψ_k) for the 16 LR images (SIs). From these plots it is shown how the average SAD measure captured the mismatch among the three outlier images and the reference LR image. It is also noted that the outlier thresholds that correspond to SIs #4 and #10 are considerably smaller because of their severe violation to the assumed translational motion model. It is observed how the influence functions that correspond to SIs #4 and #10 decay rapidly, assigning almost negligible weight to the projection errors of the corresponding LR image and hence effectively suppressing their effect in the estimation process. The HR estimate that uses the L_2 error norm [18,22] and Tikhonov regularization is shown in Fig. 5(d). From this result it is shown that the L_2 estimate suffers from noticeable artifacts that are due to the outliers (the shadows corresponding to the outlier images appear in the background). This result is not surprising, since the L_2 error norm is vulnerable to the outliers because of its linear influence function that assigns larger weights to larger errors and hence amplifies their influence on the estimation. The HR estimate that uses the L_1 error norm [22] and Tikhonov regularization is shown in Fig. 5(e). From this result it is shown how use of the L_1 error norm has suppressed the outliers compared with use of the L_2 error norm. However, as discussed earlier, because of its constant-valued influence function (± 1), it results in a blurry HR estimate of relatively poor quality. The HR estimate that uses the Lorentzian error norm [27] and Tikhonov regularization is shown in Fig. 5(f). It is shown how the effect of the outliers has been suppressed. However, the solution is blurry and of relatively poor quality because of the use of a relatively small outlier

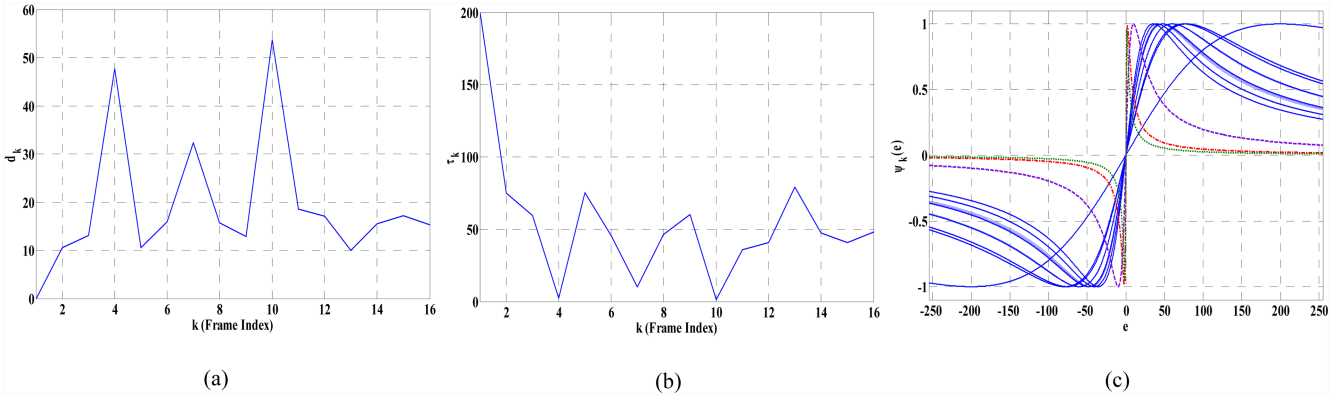

Fig. 4. (Color online) Plots of (a) average SAD values (d_k), (b) outlier thresholds (τ_k), (c) Lorentzian influence functions (ψ_k): dash–dot, dot, and dashed curves correspond to SIs #4, #10, and #7, respectively, for test sequence #1.

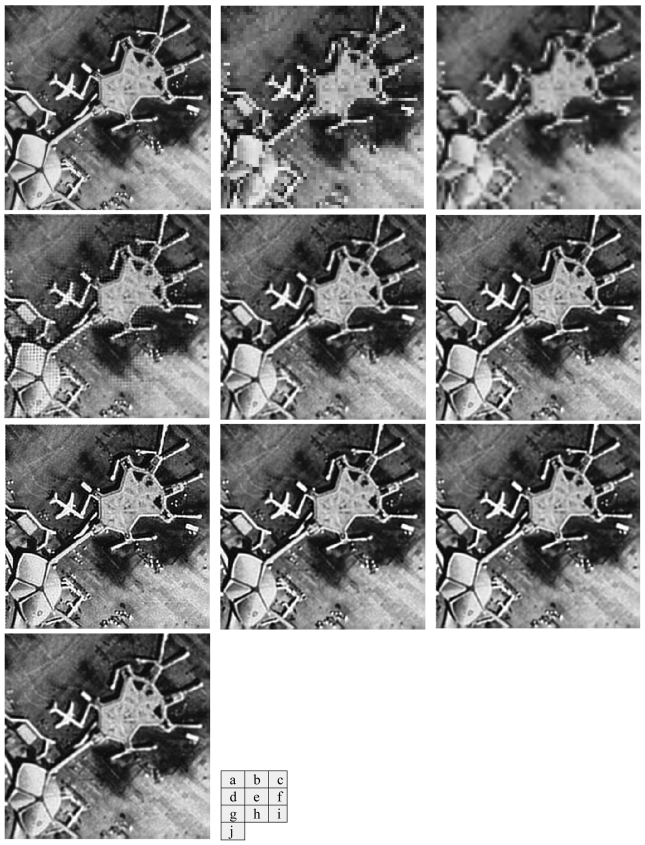

Fig. 5. 4× HR image reconstruction results for test sequence #1: a, original HR ROI; b, LR image detected by the reference SI, SI #1; c, initial estimate (bilinear interpolation of b); d, L_2 estimate + Tikhonov regularization; e, L_1 estimate + Tikhonov regularization; f, Lorentzian estimate [27] + Tikhonov regularization; g, proposed algorithm without regularization; h, proposed algorithm + regularization;, i, L_2 estimate + Tikhonov regularization, excluding SIs #4, #7, and #10 from the reconstruction process; j, L_1 estimate + Tikhonov regularization, excluding SIs #4, #7, and #10 from the reconstruction process.

threshold (to deal effectively with the outliers) and incorporating regularization. The HR reconstruction result using the proposed scheme without regularization is shown in Fig. 5(g). From this result it is observed how the proposed approach has successfully suppressed the effect of the outliers, resulting in an artifacts-free HR estimate of crisp details. Figure 5(h) depicts the HR estimate using the proposed scheme with Tikhonov regularization. The use of regularization slightly smoothed the HR estimate because of the prior imposed smoothness. Figures 5(i) and 5(j) show the HR estimate using the L_2 error norm [18,22] and Tikhonov regularization and the L_1 error norm [22] and Tikhonov regularization, respectively, if the images corresponding to SI #4, SI #7 and SI #10 were excluded (rejected) from the reconstruction process. We observed that the performance of the L_1 error norm is almost the same because of its constant-valued influence function. The L_2 error norm estimate does not suffer from any artifacts because of outlier rejection. However, because of regularization, the estimate is slightly blurred. Comparison of the two results in Figs. 5(i) and 5(h) and the proposed results (without regularization) in Fig. 5(h), it is clear that the estimate using the proposed scheme is crisper and does not suffer from any estimation artifacts because of the robust error norm used and the effective strategy for dealing with the outliers.

B. Real Experiment: 4× HR Reconstruction

Steerable MCI schemes, such as PANOPTES, are still in the implementation phase, and there are no real data available that could be used for validation. However, to demonstrate the robustness of the proposed scheme when applied to real data, we present the reconstruction results from a LR sequence taken by a single-aperture LR camera, where each LR frame in the sequence will be treated as the output from a LR SI in a steerable MCI system. Although this sequence is not an accurate representation of actual sequences to be obtained later from steerable MCIs, the promising results of the proposed scheme imply that it would be successful when applied to such systems. For this experiment we used 30 (64 × 96) frames from the Emily sequence (frames 40 through 69), which is available in the data set http://www.soe.ucsc.edu/~milanfar/DataSets. The 30 frames approximately follow the translational motion model with the last five frames including head movement and a more complicated motion. This sequence will be referred to as test sequence #2. For this sequence, a translational motion model is assumed, and the algorithm in Ref. [45] is used to estimate the motion vectors. The unknown camera PSF is assumed to be a normalized 5×5 Gaussian kernel of zero mean and unity variance. Figures 6(a) and 6(b) show LR frame #1 and LR frame #27 (including Emily's head movement), respectively.

The HR estimate using the L_2 error norm [18,22] and Tikhonov regularization is shown in Fig. 6(c). From this result it is shown that the L_2 estimate suffers from visible artifacts that are due to Emily's head movement. The HR estimate using the L_1 error norm [22] and Tikhonov regularization is shown in Fig. 6(d). From this result it is shown how use of the L_1 error norm has suppressed the outliers compared with use of the L_2 error norm. However, it again results in a blurry HR estimate. The HR estimate obtained with the Lorentzian error norm [27] and Tikhonov regularization is shown in Fig. 6(e), which shows how the effect of the outliers has not been totally suppressed and the solution is blurry and of relatively poor quality. This result is a consequence of (1) using a fixed outlier threshold for all LR frames that do not enable proper outlier suppression or rejection and (2) incorporating regularization. The HR reconstruction results using the proposed scheme without and with regularization are shown in Figs. 6(f) and 6(g), respectively. Again, it is observed how the proposed approach has successfully suppressed the effect of the

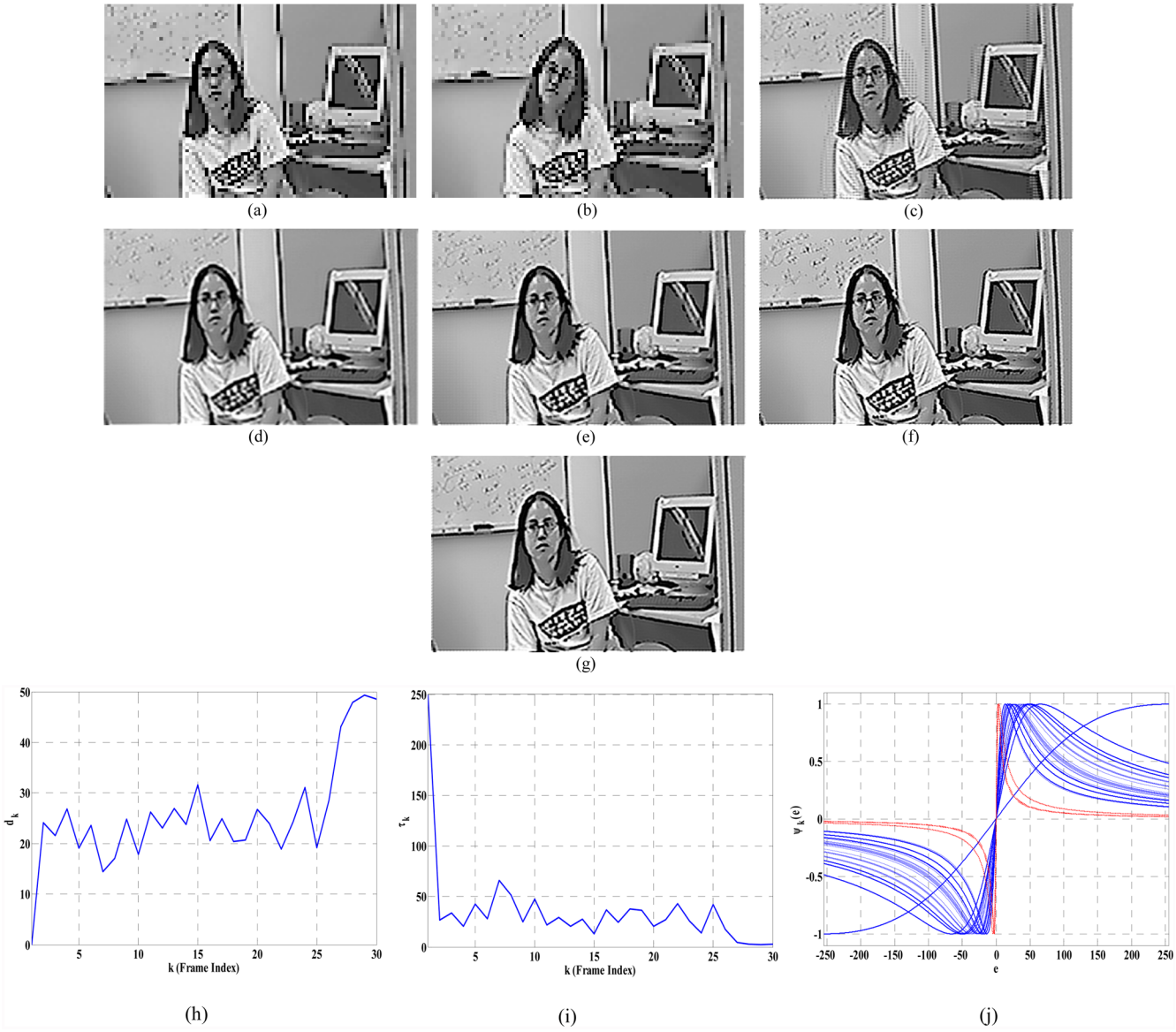

Fig. 6. (Color online) 4× HR image reconstruction results for test sequence #2: (a) LR frame #1, (b) LR frame #27, (c) L_2 estimate + Tikhonov regularization, (d) L_1 estimate + Tikhonov regularization, (e) Lorentzian estimate [27] + Tikhonov regularization, (f) proposed algorithm without regularization, (g) proposed algorithm + Tikhonov regularization, (h) plot of average SAD values (d_k), (i) plot of the outlier thresholds (τ_k), (j) plot of the Lorentzian influence functions (ψ_k): dotted curves correspond to frames 26 through 30, which include head movement.

outliers, resulting in an artifacts-free HR estimate of crisp details, even without the use of regularization. The results using regularization are slightly smoother because of the prior smoothness imposed on the solution. Plots of the average SAD (d_k), the outlier thresholds (τ_k), and the Lorentzian influence functions (ψ_k) are also depicted in Fig. 6. From these plots it can be seen how the average SAD measure was able to capture the mismatch between the reference (first) LR frame and the outlier frames in which Emily moves her head and the motion violates the translational model. It is also noted that the outlier thresholds that correspond to frames 26 through 30 are considerably small because of their violation of the assumed single translational motion model. The influence functions that correspond to frames 26 through 30 decay rapidly, assigning almost negligible weight to the projection errors of these frames and hence suppressing their effect.

5. Conclusions

We have presented an adaptive M-estimation framework for robust high-resolution image reconstruction in steerable multiplexed computational imaging systems. Use of a robust error norm and adapting the estimation process to each low-resolution image detected by each low-resolution subimager in the sensor array, the proposed method effectively suppresses the outliers that are due to model violations and results in HR estimates with

crisp details and no estimation artifacts, without the use of a regularization term in the objective function. Experimental results have demonstrated the superior performance of the proposed algorithm over methods based on the L_2, L_1, or Lorentzian error norms.

This research was funded in part through a collaborative technology agreement with the U.S. Army Research Laboratory under award W911NF-06-2-0035.

References

1. J. N. Mait, R. Athale, and J. van der Gracht, "Evolutionary paths in imaging and recent trends," Opt. Express **11**, 2093–2101 (2003).
2. J. Mait, M. W. Haney, Keith Goossen, and M. P. Christensen, "Shedding light on the battlefield: tactical applications of photonic technology," Ref. A370034 (National Defense University Center for Technology and National Security Policy, 2004).
3. P. M. Shankar, W. C. Hasenplaugh, R. L. Morrison, R. A. Stack, and M. A. Neifeld, "Multiaperture imaging," Appl. Opt. **45**, 2871–2883 (2006).
4. J. Tanida, T. Kumagai, K. Yamada, and S. Miyatake, "Thin observation module by bound optics (TOMBO): concept and experimental verification," Appl. Opt. **40**, 1806–1813 (2001).
5. M. P. Christensen, M. W. Haney, D. Rajan, S. Wood, and S. Douglas, "PANOPTES: a thin agile multi-resolutions imaging sensor," presented at the Government Microcircuit Applications and Critical Technology Conference (GOMACTech-05), Las Vegas, Nevada, 4–7 April 2005, paper 21.5.
6. M. W. Haney, M. P. Christensen, D. Rajan, S. C. Douglas, and S. L. Wood, "Adaptive flat micro-mirror-based computational imaging architecture," presented at OSA Topical Meeting on Computational Optical Sensing and Imaging (COSI), Charlotte, North Carolina, 6–9 June 2005.
7. M. P. Christensen, V. Bhakta, D. Rajan, T. Mirani, S. C. Douglas, S. L. Wood, and M. W. Haney, "Adaptive flat multiresolution multiplexed computational imaging architecture utilizing micromirror arrays to steer subimager fields of view," Appl. Opt. **45**, 2884–2892 (2006).
8. H.-B. Lan, S. L. Wood, M. P. Christensen, and D. Rajan, "Benefits of optical system diversity for multiplexed image reconstruction," Appl. Opt. **45**, 2859–2870 (2006).
9. K. Aizawa, T. Komatsu, and T. Saito, "A scheme for acquiring very high resolution images using multiple cameras," IEEE Trans. Acoust. Speech Signal Process. **3**, 23–26 (1992).
10. S. C. Park, M. K. Park, and M. G. Kang, "Super-resolution image reconstruction: a technical overview," IEEE Signal Process. Mag. **20** (3), 21–36 (2003).
11. S. Chaudhuri, *Super-Resolution Imaging* (Norwell, 2001).
12. R. Y. Tsai and T. S. Huang, "Multiframe image restoration and registration," in *Advances in Computer Vision and Image Processing*, T.S.Huang, ed. (JAI Press, 1984), Vol. 1, pp. 317–339.
13. H. Ur and D. Gross, "Improved resolution from subpixel shifted pictures," CVGIP Graph. Models Image Process. **54**, 181–186 (1992).
14. M. Irani and S. Peleg, "Improving resolution by image registration," CVGIP Graph. Models Image Process. **53**, 231–239 (1991).
15. R. C. Hardie, K. J. Barnard, J. G. Bognar, E. E. Armstrong, and E. A. Watson, "High-resolution image reconstruction from a sequence of rotated and translated frames and its application to an infrared imaging system," Opt. Eng. **37**, 247–260 (1998).
16. M. Elad and A. Feuer, "Restoration of a single superresolution image from several blurred, noisy, and undersampled measured images," IEEE Trans. Image Process. **6**, 1646–1658 (1997).
17. M. Elad and Y. Hel-Or, "A fast super-resolution reconstruction algorithm for pure translation motion and common space-invariant blur," IEEE Trans. Image Process. **10**, 1187–1193 (2001).
18. A. Zomet and S. Peleg, "Efficient super-resolution and applications to mosaics," in *15th International Conference on Pattern Recognition, 2000* (2000), Vol. **1**, pp. 579–583,.
19. A. Zomet, A. Rav-Acha, and S. Peleg, "Robust super-resolution," in *Proceedings of the 2001 IEEE Computer Society Conference on Computer Vision and Pattern Recognition, 2001*, Vol. **1**, I-645–I-650 (2001).
20. N. Nguyen, P. Milanfar, and G. Golub, "A computationally efficient super-resolution image reconstruction algorithm," IEEE Trans. Image Process. **10**, 573–583 (2001).
21. S. Farsiu, D. Robinson, M. Elad, and P. Milanfar, "Robust shift and add approach to super-resolution," Proc. SPIE **5203**,121–130 (2003).
22. S. Farsiu, D. Robinson, M. Elad, and P. Milanfar, "Fast and robust multi-frame super-resolution," IEEE Trans. Image Process. **13**, 1327–1344 (2004).
23. E. S. Lee and M. G. Kang, "Regularized adaptive high-resolution image reconstruction considering inaccurate subpixel registration," IEEE Trans. Image Process. **12**, 826–837 (2003).
24. M. V. W. Zibetti and J. Mayer, "Outlier robust and edge-preserving simultaneous super-resolution," in *IEEE International Conference on Image Processing*, 1741 –1744 (2006).
25. M. Trimeche, R. C. Bilcu, and J. Yrjänäinen, "Adaptive outlier rejection in image super-resolution", EURASIP J. Appl. Signal Process. **2006**, 38052 (2006).
26. D. Capel, *Image Mosaicing and Super-resolution* (Springer, 2004).
27. V. Patanavijit and S. Jitapunkul, "A Lorentzian stochastic estimation for a robust iterative multiframe super-resolution reconstruction with Lorentzian–Tikhonov regularization," EURASIP J. Adv. Signal Process. **2007**, 34821 (2007).
28. N. A. El-Yamany and P. E. Papamichalis are preparing a manuscript to be called "Using bounded-influence M-estimators in multiframe super-resolution reconstruction: a comparative study."
29. N. A. El-Yamany and P. E. Papamichalis, "An adaptive M-estimation framework for robust image super-resolution without regularization," to appear in *SPIE Conference on Visual Communications and Image Processing* (VCIP), San Jose, California, 2008.
30. N. A. El-Yamany, P. E. Papamichalis, and W. R. Schucany, "A robust image super-resolution scheme based on redescending M-estimators and information-theoretic divergence," in *Proceedings of the IEEE International Conference on Acoustics, Speech and Signal Processing* (ICASSP), Honolulu, Hawaii (2007).
31. N. A. El-Yamany and P. E. Papamichalis, "Robust color image super-resolution: an adaptive M-estimation framework," EURASIP J. Image Video Process. (2008).
32. T. Q. Pham, L. J. van Vliet, and K. Schutte, "Robust super-resolution by minimizing a Gaussian-weighted L_2 error norm," J. Phys. Conf. Ser., to be published.
33. Z. A. Ivanovski, L. Panovski, and L. J. Karam, "Robust super-resolution based on pixel-level selectivity", Proc. SPIE **6077**, 607707 (2006).
34. W. Zhao and H. S. Sawhney, "Is super-resolution with optical flow feasible?," in *Proceedings of the 7th European Conference on Computer Vision-Part I*, A. Heyden, G. Sparr, M. Nielsen, and P. Johansen, eds. (Springer-Verlag, 2002), pp. 599–613.

35. P. J. Huber, *Robust Statistics*, Wiley Series in Probability and Statistics (Wiley-Interscience, 2003).
36. F. R. Hampel, E. M. Ronchetti, P. J. Rousseeuw, and W. A. Stahel, *Robust Statistics: the Approach Based on Influence Functions*, Wiley Series in Probability and Statistics (Wiley-Interscience, 2005).
37. R. A. Maronna, D. R. Martin, and V. J. Yohai, *Robust Statistics: Theory and Methods*, Wiley Series in Probability and Statistics (Wiley, 2006).
38. N. Sebe and M. S. Lew, *Robust Computer Vision: Theory and Applications* (Springer, 2003).
39. P. Meer, D. Mintz, A. Rosenfeld, and D. Y. Kim, "Robust regression methods for computer vision: a review," Int. J. Comput. Vision **6**, 59–70 (1991).
40. M. J. Black and P. Anandan, "The robust estimation of multiple motions: parametric and piecewise-smooth flow fields," Comput. Vision Image Understand. **63**(1), 75–104 (1996).
41. T. Rabie, "Robust estimation approach for blind denoising," IEEE Trans. Image Process. **14**, 1755–1765 (2005).
42. M. J. Black, G. Sapiro, D H. Marimont, and D. Heeger, "Robust anisotropic diffusion," IEEE Trans. Image Process. **7**, 421–432 (1998).
43. D. P. Bertsekas, *Nonlinear Programming* (Athena Scientific, 1999).
44. A. Blake and A. Zisserman, *Visual Reconstruction* (MIT Press, 1987).
45. J. R. Bergen, P. Anandan, K. J. Hanna, and R. Hingorani, "Hierarchical model-based motion estimation," in *Proceedings of the European Conference on Computer Vision* (Springer-Verlag, 1992), pp. 237–252.